Coherent control of a surface structural phase transition

Jan Gerrit Horstmann[1], Hannes Böckmann[1], Bareld Wit[1], Felix Kurtz[1], Gero Storeck[1], and Claus Ropers[1,2]*

[1]4th Physical Institute, Solids and Nanostructures, University of Göttingen, Göttingen 37077, Germany.
[2]Max Planck Institute for Biophysical Chemistry, Göttingen 37077, Germany.

The desire to exert active optical control over matter is a unifying theme across multiple scientific disciplines, as exemplified by all-optical magnetic switching[1,2], light-induced metastable or exotic phases of solids[3–8] and the coherent control of chemical reactions[9,10]. Typically, these approaches dynamically steer a system towards states or reaction products far from equilibrium. In solids, metal-insulator transitions are an important target for optical manipulation, offering dramatic and ultrafast changes of the electronic[4] and lattice[11–16] properties. In this context, essential questions concern the role of coherence in the efficiencies and thresholds of such transitions. Here, we demonstrate coherent control over a metal-insulator structural phase transition in a quasi-one-dimensional solid-state surface system. A femtosecond double-pulse excitation scheme[17–20] is used to drive the system from the insulating to a metastable metallic state, and the corresponding structural changes are monitored by ultrafast low-energy electron diffraction[21,22]. We harness vibrational coherence in key structural modes to govern the transition, as evidenced by delay-dependent oscillations in the double-pulse switching efficiency. Mode-selective coherent control of solids and surfaces could open new routes to switching chemical and physical functionalities, facilitated by metastable and non-equilibrium states.

Femtochemistry entails the search for understanding and control of ultrafast reaction pathways[9,20]. To this end, coherences in the electronic and vibrational states of reactants are employed to affect transitions in a complex, generally multidimensional energy landscape[9,23]. Established for small molecules, a possible transfer of this concept to extended systems and solids is complicated, e.g. due to a high electronic and vibrational density of states, and couplings to an external heat bath. Low-dimensional and strongly correlated systems represent a promising intermediate between molecules and solids, with phase transitions assuming the role of a

"reaction." A number of these transitions can be driven optically - either by means of transient heating[22,24], electronic excitation[13–16,25,26] or direct resonant coupling to certain vibrational degrees of freedom[4–6]. The prototypical case of a phase transition governed by structural modes is given by the Peierls instability[27], in which a metal-to-insulator transition (MIT) is linked to phonon softening and the appearance of a static periodic lattice distortion (PLD). Coherent oscillations of the PLD, so-called amplitude modes or amplitudons, are frequently observed in the optical pumping of such transitions, especially close to their threshold[28–33]. In analogy to the vibrational spectroscopy of reacting molecules[34], amplitudons can be used to track ultrafast changes in the lattice symmetry across a phase transition[29,32,33]. However, it remains to be shown how coherent amplitude motion can be utilized to manipulate the outcome of a structural transition.

Here, we report coherent control over the phase transition in a quasi-one-dimensional Peierls insulator via the amplitudes of decisive phonon modes. We employ a double-pulse excitation scheme and monitor the structural transformation by ultrafast low-energy electron diffraction (ULEED; Fig. 1a, see Methods)[21,22]. Observing the resulting structure as a function of the double-pulse separation demonstrates the importance of shear and rotational phonon modes on the femtosecond timescale. A comparison of ULEED and transient reflectivity measurements suggests distinct roles of these phonons in controlling the transition, and points to the location of the transition state along the mode coordinates.

As a model system, we study atomic indium wires on the Si(111) surface[35], a prominent Peierls system attracting significant interest for its ultrafast dynamics[13–16]. Arranged in a "zigzag" pattern, the indium atoms induce a metallic (4×1) superstructure, which, at $T_c = 125$ K, exhibits a first-order transition to an insulating state with quadrupled (8×2) unit cell size and a "hexagon"-shaped indium pattern. The associated change in atomic structure causes additional spots in backscattering diffraction (cf. LEED patterns in Fig. 1b). Below T_c, a single optical pump pulse is able to electronically excite the system to a metastable (4×1) state[13–16]. Recently, time-resolved diffraction and photoemission spectroscopy revealed the ultrafast and ballistic nature of this transition (occuring on a 350-fs timescale) and identified excited electrons and localized photoholes as its driving force[14–16].

Tracking the (4×1)/(8×2) diffraction spot intensities in ULEED, we observe a rapid increase/decrease directly after optical excitation and subsequent relaxation to a level persisting

over nanoseconds (Fig. 1c, left), evidencing the metastability of the structure[13]. Interestingly, this long-lived contribution displays a rather gradual threshold in pump fluence. This implies that for intermediate excitation densities, a variable part of the surface is switched to the metastable state (Fig. 1c, right), despite a homogeneous excitation of the probed area (see Methods). An interpretation based on the coexistence of both phases is also corroborated by scanning tunneling microscopy[36] and Raman spectroscopy[37] well below T_c.

It may be anticipated that near the threshold, the structural transition is particularly susceptible to weak perturbations, affecting the efficiency of driving the system to the metastable state. Motivated by control schemes in femtochemistry[17–20], we explore the use of pulse sequences to manipulate the switching efficiency. Specifically, we employ a pair of optical pump pulses with variable delay $\Delta t_{p\text{-}p}$, and probe the resulting structure by ULEED at a later time of $\Delta t_{p\text{-}el} = 75$ ps, well after the excitation. We find that the signature of the metastable state, i.e., a suppression/increase of the (8×2)/(4×1) phase, is a strong function of the double-pulse delay $\Delta t_{p\text{-}p}$ (Fig.2a). Importantly, at intermediate fluences between 0.5 and 1.4 mJ cm^{-2}, pronounced oscillations with a period of 1-2 ps are observed on either delay side, with opposing behavior for the (4×1) (top panel) and (8×2) spots. In contrast, only a minor delay-dependence is found well below and above threshold. The peaked signal around $\Delta t_{p\text{-}p} = 0$ is attributed to additive electronic excitation which decays on a few-picosecond timescale[38].

The observed oscillations clearly demonstrate a coherent response of the signal. In particular, coherent vibrational motion induced by the first pulse controls the switching efficiency for the second pulse. The frequency content of the signal (Fig. 2b, top) points to shear and rotation phonon modes, which have previously been identified as amplitude modes of the metal-insulator phase transition[37,39] (see Fig.2c). Interestingly, Fourier-filtered traces of the two observed frequency bands exhibit opposite phases at time zero, corresponding to enhancement or suppression of the transition for pulse overlap (see Fig. 2b, bottom).

The appearance of coherent phonons is understood within the established potential energy model of the transition[13,14,39,40]. The (8×2)→(4×1) transformation is typically described in terms of a tristable energy surface, with an initial minimum at the (8×2) configuration. Electronic excitation tilts the balance towards the (4×1) phase (Fig. 3a)[13–15,40], accompanied by displacive

excitation of coherent phonons (DECP)[25]. The question now arises how these phonon coherences facilitate control over the transition.

Generally, Raman-active phonons can modulate the optical absorption of a surface[25,29], affecting the level of electronic excitation achieved by the second pulse. This can influence the final-state potential energy surface and the observed threshold ("absorption control", see Fig. 3c). Amplitude modes of the symmetry-broken state are expected to facilitate this mechanism, given their direct link to the structural transformation and their susceptibility to strong displacive excitation. Moreover, the ballistic nature of the transition[14] and the significant influence of DECP suggests that kinetic energy contributes to overcoming a sufficiently lowered but not completely vanishing barrier ("ballistic control", see Fig. 3b). For the vibrational motion along a reaction coordinate, in-phase excitation with a second pulse maximizes the effect of DECP and allows for a barrier-crossing to the (4×1) state (1). Anti-phase excitation, on the other hand, vibrationally de-excites the system, which then has insufficient kinetic energy and remains in the (8×2) state (2). In a corresponding real-space picture, by weakening/strengthening different In-In bonds[15] and thus shifting the equilibrium atomic positions, the second pulse either adds further mechanical stress to the system (1), or removes it (2). While the absorption modulation described above may apply to all Raman-active modes q[25], this ballistic contribution is only feasible for modes along the reaction coordinate Q.

To further elucidate the contributions of these mechanisms, we complement ULEED by optical pump-probe (OPP) spectroscopy (see Methods section for details), which probes absorption modulation by coherent phonons[25]. We measure pump-induced changes in the optical reflectivity, which are directly proportional to absorption changes for a monolayer on a substrate with real refractive index[41]. A comparison of the switching efficiency (Fig. 3d) with the transient reflectivity (Fig. 3e) reveals both similarities and stark differences in the observed frequencies and their relative amplitudes (see also Extended Data Fig. 6 for further OPP traces).

Both measurements exhibit a frequency component close to 0.82 THz, which we assign to the hexagon rotation mode of the (8×2) structure[37,39]. Due to its anti-phase behaviour at $\Delta t_{p\text{-}p} = 0$ (see Fig.2b), for this mode, a ballistic control mechanism can be ruled out. We therefore attribute the rotation-mode ULEED signal to absorption modulation. This assignment is further corroborated by the modulation amplitudes in both types of measurements, which are linked through the total

absorption of the monolayer. Our measurements predict a value of about 1 %, similar to a recent estimate[16] (see Methods).

A more intricate situation is found for the low-frequency component, associated with shear phonons: This dominant feature in ULEED modulates the switching efficiency to a disproportionately higher degree than expected from the overall transient reflectivity. Moreover, the shear mode frequencies measured by ULEED (0.57 THz) and OPP (0.64 THz) differ significantly. This may be a result of OPP probing a surface-averaged optical response, while ULEED is sensitive to the transition probability in regions close to threshold. However, density functional theory (DFT) and Raman spectroscopy in fact predict two separate shear modes: Whereas the *symmetric* shear mode (expected at 0.66 THz) is much more prominent in Raman spectra[37], only the *antisymmetric* shear mode (0.55 THz) is considered relevant for the transition[42,43]. These distinct properties suggest that OPP and ULEED each mainly probe a different one of these modes, namely the higher-frequency symmetric and the lower-frequency antisymmetric shear oscillation, respectively.

From these considerations, we extract two possible scenarios for the role of shear motion, linked to the control mechanisms discussed above (Fig. 3). First, if the transition is indeed driven by a shear mode *separate* from that seen in reflectivity, we have to invoke the ballistic mechanism (Fig. 3b) to explain the ULEED data, directly linking this mode to the reaction coordinate. Alternatively, in order to identify the shear contributions in ULEED and OPP with the *same* mode and absorption modulation (Fig. 3c), the observed frequency difference requires further explanation. In particular, this would necessitate a drastically softened and larger-amplitude shear mode oscillation only in surface regions that can be switched by the second pulse, with an unaltered rotation frequency (Fig. 3d).

Interestingly, both scenarios imply that the shear displacement corresponds to the primary reaction coordinate, while the rotation completing the transition[39,42] is of a secondary nature. Accordingly, we propose a description of the transition in terms of a two-dimensional potential energy surface (PES) spanned by the rotation and shear deformations of the (4×1) structure (Fig. 4a), with the system initially residing in the (8×2) minimum. In a reasonable assumption, the first pulse induces a displacive excitation of coherent phonons towards the (4×1) state. The ULEED measurements show that the transition efficiency for the second pulse becomes a strong

function of the momentary vibrational state (Fig. 4b), denoted by the colour-coded area in Fig. 4b. The combined observations, i.e., the differences in frequency and relative amplitudes between ULEED and OPP, as well as the phases of both modes in the double-pulse traces (Fig. 2b), now suggest an "off-diagonal" transition state in configuration space with a strongly reduced shear but a largely unaltered rotation (compared to the (8×2) state). This interpretation is further supported by the transient softening and hardening (Fig. 3d) of the shear and rotation mode, respectively, near $\Delta t_{p\text{-}p} = 0$ (Fig. 3d), which we have consistently observed in a number of experiments (see Extended Data Fig. 7).

In the proposed pathway of the transition, overcoming an "early" barrier[23], the In-chains are first unsheared and subsequently transformed into the zigzag structure by a rotation. It should be noted that such a pathway transiently passes the so-called "trimer" state[43,44], which has been intensely studied by density functional theory and is expected to be almost energetically degenerate to the (4×1) state[45]. The existence of two local minima for a similar rotation displacement, namely the trimer and the (8×2) configuration[45], also supports the existence of a transition state along the shear axis.

Future experimental and theoretical studies, involving DFT and molecular dynamics simulations, may further elucidate the PES, possible additional pathways and the sequential nature of the transition. With regard to these points, the microscopic excitation mechanism underlying the phonon coherences deserves further consideration, including its link to the femtosecond electron transfer and hole-induced driving forces recently described[15]. Finally, considering the surface heterogeneity, the influence of frequency changes at domain boundaries[36] on the local transition dynamics will be a subject of interest.

In conclusion, we have demonstrated the coherent control of a surface structural phase transition by all-optical manipulation of key phonon modes. Our results show that the outcome of the phase transition, much like many chemical reactions, depends on the momentary state of the coherent vibrational wavepacket. Close to the transition threshold, both absorption modulation by Raman-active modes and the ballistic motion of the order parameter in overcoming the barrier should be considered. The latter contribution could be enhanced with mode-selectivity by a repeated stimulation of the coherent phonon amplitude, which, as in the present system, decays slower than the electronic excitation[18,46].

In molecular chemistry, it has long been known that vibrational excitation and the location of the transition state may drastically affect reaction rates, a fundamental principle captured by the Polanyi rules[23]. Our work extends this principle to surfaces and solids and introduces the vibrational phase as a decisive parameter to target the transition state. We believe that exploiting vibrational coherences in low-dimensional and strongly correlated materials, as well as molecular adsorbates, holds promise for structural and electronic control in surface physics and chemistry, providing a handle to steer physical functionality and chemical reactivity.

References

1. Kimel, A. V. *et al.* Ultrafast non-thermal control of magnetization by instantaneous photomagnetic pulses. *Nature* **435**, 655–657 (2005).
2. Schlauderer, S. *et al.* Temporal and spectral fingerprints of ultrafast all-coherent spin switching. *Nature* **569**, 383 (2019).
3. Stojchevska, L. *et al.* Ultrafast switching to a stable hidden quantum state in an electronic crystal. *Science* **344**, 177–180 (2014).
4. Rini, M. *et al.* Control of the electronic phase of a manganite by mode-selective vibrational excitation. *Nature* **449**, 72–74 (2007).
5. Mitrano, M. *et al.* Possible light-induced superconductivity in K_3C_{60} at high temperature. *Nature* **530**, 461–464 (2016).
6. Nova, T. F., Disa, A. S., Fechner, M. & Cavalleri, A. Metastable ferroelectricity in optically strained $SrTiO_3$. *Science* **364**, 1075–1079 (2019).
7. Sie, E. J. *et al.* An ultrafast symmetry switch in a Weyl semimetal. *Nature* **565**, 61 (2019).
8. Wang, Y. H., Steinberg, H., Jarillo-Herrero, P. & Gedik, N. Observation of Floquet-Bloch states on the surface of a topological insulator. *Science* **342**, 453–457 (2013).
9. Zewail, A. H. Femtochemistry: Atomic-scale dynamics of the chemical bond using ultrafast lasers (Nobel lecture). *Angew. Chem. Int. Ed.* **39**, 2586–2631 (2000).
10. Nuernberger, P., Vogt, G., Brixner, T. & Gerber, G. Femtosecond quantum control of molecular dynamics in the condensed phase. *Phys. Chem. Chem. Phys.* **9**, 2470–2497 (2007).
11. Morrison, V. R. *et al.* A photoinduced metal-like phase of monoclinic VO_2 revealed by ultrafast electron diffraction. *Science* **346**, 445–448 (2014).
12. Liu, M. *et al.* Terahertz-field-induced insulator-to-metal transition in vanadium dioxide metamaterial. *Nature* **487**, 345–348 (2012).
13. Wall, S. *et al.* Atomistic picture of charge density wave formation at surfaces. *Phys. Rev. Lett.* **109**, 186101 (2012).
14. Frigge, T. *et al.* Optically excited structural transition in atomic wires on surfaces at the quantum limit. *Nature* **544**, 207–211 (2017).

15. Nicholson, C. W. *et al.* Beyond the molecular movie: Dynamics of bands and bonds during a photoinduced phase transition. *Science* **362**, 821–825 (2018).
16. Chávez-Cervantes, M., Krause, R., Aeschlimann, S. & Gierz, I. Band structure dynamics in indium wires. *Phys. Rev. B* **97**, 201401 (2018).
17. Hase, M., Fons, P., Mitrofanov, K., Kolobov, A. V. & Tominaga, J. Femtosecond structural transformation of phase-change materials far from equilibrium monitored by coherent phonons. *Nat. Commun.* **6**, 8367 (2015).
18. Weiner, A. M., Leaird, D. E., Wiederrecht, G. P. & Nelson, K. A. Femtosecond pulse sequences used for optical manipulation of molecular motion. *Science* **247**, 1317–1319 (1990).
19. Feurer, T., Vaughan, J. C. & Nelson, K. A. Spatiotemporal coherent control of lattice vibrational waves. *Science* **299**, 374–377 (2003).
20. Potter, E. D., Herek, J. L., Pedersen, S., Liu, Q. & Zewail, A. H. Femtosecond laser control of a chemical reaction. *Nature* **355**, 66 (1992).
21. Gulde, M. *et al.* Ultrafast low-energy electron diffraction in transmission resolves polymer/graphene superstructure dynamics. *Science* **345**, 200–204 (2014).
22. Vogelgesang, S. *et al.* Phase ordering of charge density waves traced by ultrafast low-energy electron diffraction. *Nat. Phys.* **14**, 184–190 (2018).
23. Polanyi, J. C., Wong, W. H. & Mok, M. H. Location of energy barriers. *J. Chem. Phys.* **51**, 1439–1469 (1969).
24. Haupt, K. *et al.* Ultrafast metamorphosis of a complex charge-density wave. *Phys. Rev. Lett.* **116**, 016402 (2016).
25. Zeiger, H. J. *et al.* Theory for displacive excitation of coherent phonons. *Phys. Rev. B* **45**, 768–778 (1992).
26. Sciaini, G. *et al.* Electronic acceleration of atomic motions and disordering in bismuth. *Nature* **458**, 56–59 (2009).
27. Peierls, R. E. *Quantum theory of solids*. (Oxford University Press, 2001).
28. Eichberger, M. *et al.* Snapshots of cooperative atomic motions in the optical suppression of charge density waves. *Nature* **468**, 799–802 (2010).

29. Wall, S. *et al.* Ultrafast changes in lattice symmetry probed by coherent phonons. *Nat. Commun.* **3**, 721 (2012).
30. Sokolowski-Tinten, K. *et al.* Femtosecond X-ray measurement of coherent lattice vibrations near the Lindemann stability limit. *Nature* **422**, 287–289 (2003).
31. Rettig, L., Chu, J.-H., Fisher, I. R., Bovensiepen, U. & Wolf, M. Coherent dynamics of the charge density wave gap in tritellurides. *Faraday Discuss.* **171**, 299–310 (2014).
32. Beaud, P. *et al.* A time-dependent order parameter for ultrafast photoinduced phase transitions. *Nat. Mater.* **13**, 923–927 (2014).
33. Neugebauer, M. J. *et al.* Optical control of vibrational coherence triggered by an ultrafast phase transition. *Phys. Rev. B* **99**, 220302 (2019).
34. Nibbering, E. T. J., Fidder, H. & Pines, E. Ultrafast Chemistry: Using time-resolved vibrational spectroscopy for interrogation of structural dynamics. *Annu. Rev. Phys. Chem.* **56**, 337–367 (2005).
35. Yeom, H. W. *et al.* Instability and charge density wave of metallic quantum chains on a silicon surface. *Phys. Rev. Lett.* **82**, 4898–4901 (1999).
36. Song, S. K., Samad, A., Wippermann, S. & Yeom, H. W. Dynamical Metal to Charge-Density-Wave Junctions in an Atomic Wire Array. *Nano Lett.* **19**, 5769–5773 (2019).
37. Speiser, E., Esser, N., Wippermann, S. & Schmidt, W. G. Surface vibrational Raman modes of In:Si(111) (4×1) and (8×2) nanowires. *Phys. Rev. B* **94**, 075417 (2016).
38. Nicholson, C. W. *et al.* Excited-state band mapping and momentum-resolved ultrafast population dynamics in In/Si(111) nanowires investigated with XUV-based time- and angle-resolved photoemission spectroscopy. *Phys. Rev. B* **99**, 155107 (2019).
39. Wippermann, S. & Schmidt, W. G. Entropy explains metal-insulator transition of the Si(111)-In nanowire array. *Phys. Rev. Lett.* **105**, 126102 (2010).
40. Jeckelmann, E., Sanna, S., Schmidt, W. G., Speiser, E. & Esser, N. Grand canonical Peierls transition in In/Si(111). *Phys. Rev. B* **93**, 241407 (2016).
41. Li, Y. & Heinz, T. F. Optical models for thin layers. *ArXiv180100402 Cond-Mat physics.optics* (2018).
42. Wippermann, S. Understanding substrate-supported atomic-scale nanowires from ab initio theory. (University of Paderborn, 2010).

43. Stekolnikov, A. A. *et al.* Hexagon versus Trimer Formation in In Nanowires on Si(111): Energetics and Quantum Conductance. *Phys. Rev. Lett.* **98**, 026105 (2007).
44. Kumpf, C. *et al.* Low-Temperature Structure of Indium Quantum Chains on Silicon. *Phys. Rev. Lett.* **85**, 4916–4919 (2000).
45. González, C., Ortega, J. & Flores, F. Metal–insulator transition in one-dimensional In-chains on Si(111): combination of a soft shear distortion and a double-band Peierls instability. *New J. Phys.* **7**, 100–100 (2005).
46. Nelson, K. A. The prospects for impulsively driven, mode-selective chemistry in condensed phases. in *Mode Selective Chemistry* (eds. Jortner, J., Levine, R. D. & Pullman, B.) 527–533 (Springer Netherlands, 1991).

Acknowledgements This work was funded by the European Research Council (ERC Starting Grant 'ULEED', ID: 639119) and the Deutsche Forschungsgemeinschaft (SFB-1073, project A05). We gratefully acknowledge insightful discussions with N. S. Kozák, H. Schwoerer, R. Ernstorfer, M. Wolf, A. M. Wodtke, and M. Horn-von Hoegen. We further acknowledge constructive and insightful input from the Reviewers.

Author Contributions The project was conceived by C.R., with contributions from J.G.H. Experiments and data analysis were conducted by J.G.H., with contributions from H.B., B.W., G.S. and F.K. The manuscript was written by J.G.H., H.B. and C.R. All authors discussed the results and commented on the manuscript.

Competing interests The authors declare no competing financial interests.

Additional information Correspondence and requests for materials should be addressed to C. Ropers (cropers@gwdg.de).

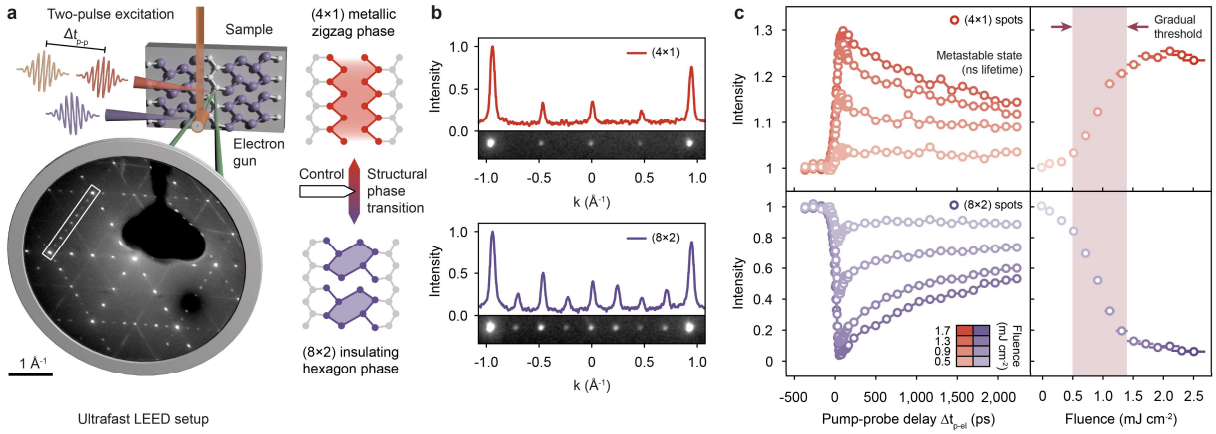

Figure 1 | Ultrafast LEED setup and structural phase transition in atomic indium wires on silicon.

a, Experimental scheme. Ultrashort electron pulses from a miniaturized laser-driven electron gun are utilized in a LEED experiment to monitor the microscopic structure of atomic indium wires on the Si(111) surface after optical excitation with single or double pulses. **b,** Cutouts and line profiles from LEED patterns of the metallic (4×1) and insulating (8×2) phases (white frame in (a)). The emergence of additional spots in the (8×2) phase indicates the pronounced structural changes during the phase transition. **c**, (Left) Time-resolved integrated intensities of (4×1) and (8×2) diffraction spots as a function of the pump-probe delay $\Delta t_{p\text{-}el}$. (Right) Fluence-dependent spot intensities recorded at $\Delta t_{p\text{-}el} = 75$ ps. The (4×1) and (8×2) intensities have been normalized to corresponding values at $\Delta t_{p\text{-}el} < 0$.

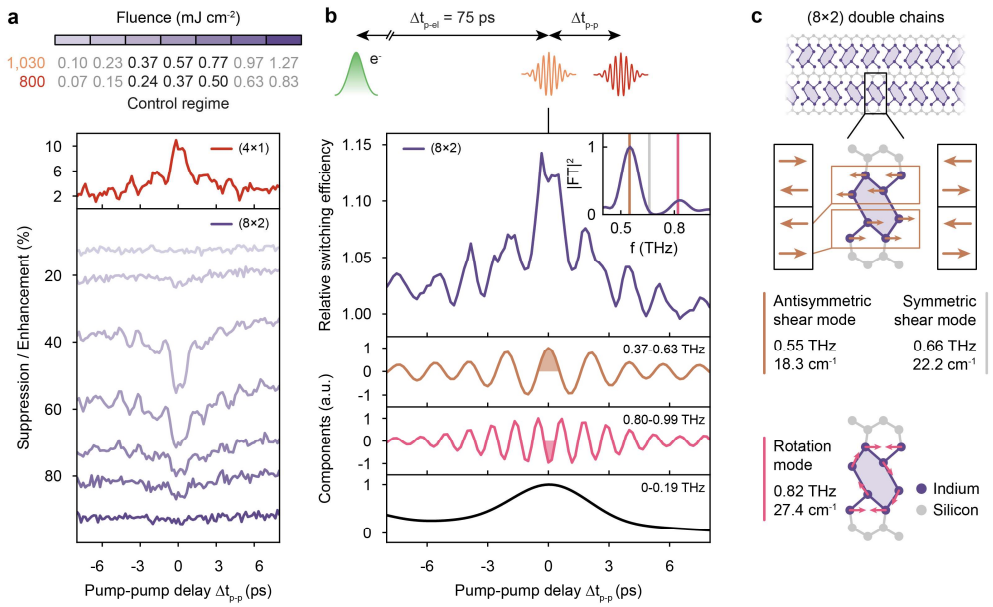

Figure 2 | Coherent control of the (8×2)→(4×1) phase transition efficiency.

a, Suppression/enhancement of the integrated (8×2)/(4×1) diffraction spot intensity as a function of the double-pulse delay $\Delta t_{p\text{-}p}$ and incident fluence F; (4×1) trace: $F_{1030} = 0.37$ mJ cm^{-2}, $F_{800} = 0.24$ mJ cm^{-2}. **b**, (Top) Delay-dependent relative switching efficiency for $F_{1030} = 0.32$ mJ cm^{-2}, $F_{800} = 0.21$ mJ cm^{-2}. Inset: Spectral density of switching efficiency; vertical lines represent the frequencies of structural modes given in (c). (Bottom) Fourier-filtered contributions of different frequency components. a.u., arbitrary units. **c**, Prominent low-frequency modes of the (8×2) structure.

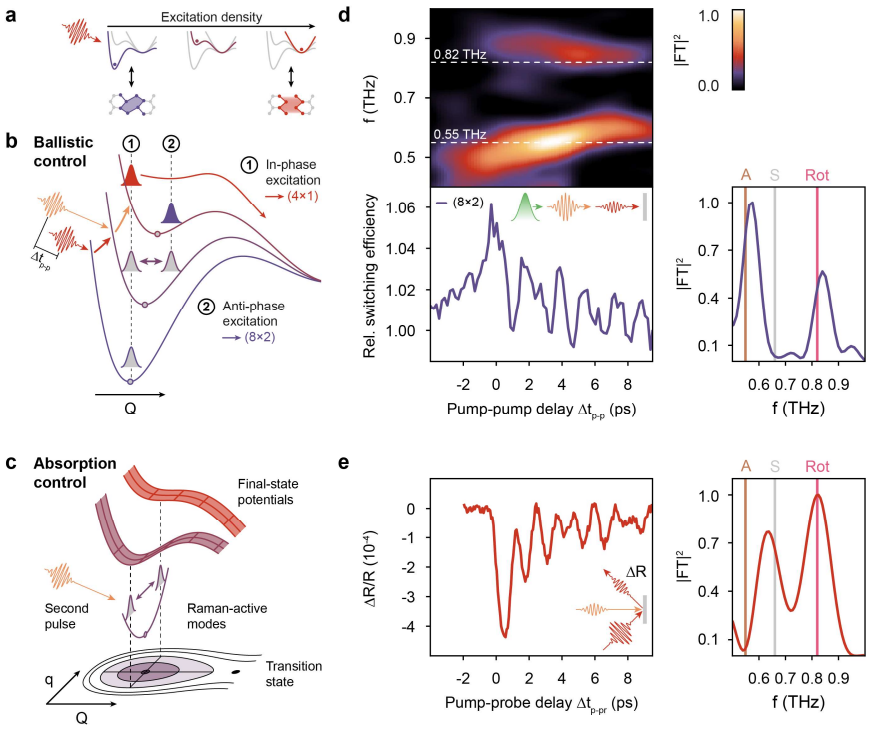

Figure 3 | Control mechanisms and comparison between ULEED and optical pump-probe spectroscopy.
a, Phase transition model based on reshaping of the tristable energy surface by a single pump pulse. For simplicity, the second, energetically degenerate (8×2) minimum is not depicted. Note that the potential deformation is a continuous function of the excitation density. **b**, **c**, Coherent control mechanisms in double-pulse experiments: ballistic control (b) and absorption control (c). **d**, Relative switching efficiency recorded for unequal pump pulses in ULEED (F_{1030} = 0.48 mJ cm^{-2}, F_{800} = 0.15 mJ cm^{-2}), corresponding spectral density (right) with reference frequencies (see Fig.2c) and short-time Fourier transform (top). “A”, “S”, and “Rot” indicate the frequencies of antisymmetric, symmetric and rotation modes, respectively. **e**, Delay-dependent reflectivity changes $\Delta R/R$ of the surface measured in optical pump-probe experiments and corresponding spectral density (F_{pump} = 0.15 mJ cm^{-2}).

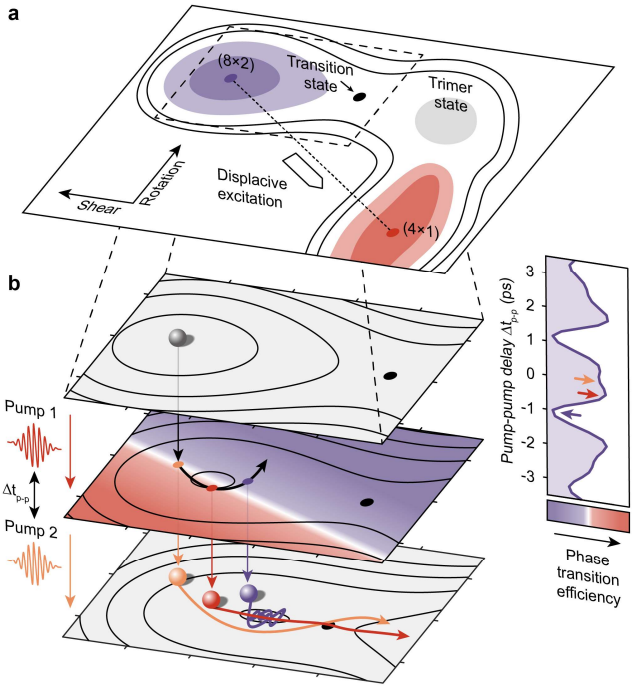

Figure 4 | Two-dimensional picture of the phase transition dynamics.

a, Proposed two-dimensional model of the potential energy surface (PES) for the (8×2)→(4×1) in shear/rotation configuration space, exhibiting a transition state along the shear axis from the (8×2) state. **b**, Sketch of exemplary system trajectories close to the (8×2) state before (top), in between (middle) and after (bottom) two subsequent displacive excitations (yellow: $\Delta t_{p\text{-}p} = 0$, red: $\Delta t_{p\text{-}p} \approx T_{rot}/2$, violet: $\Delta t_{p\text{-}p} \approx T_{shear}/2$). The phase transition efficiency (colour coded) is a strong function of the vibrational coordinates at the time of the second pulse (middle and right panel). Highest efficiency is achieved for a maximum sheared/minimum rotated structure (see middle panel).

Methods

Ultrafast LEED setup. We recently developed ultrafast low-energy electron diffraction (ULEED) in an optical-pump/electron probe scheme for the time-resolved investigation of structural dynamics at solid state surfaces[21,22,47]. LEED is a surface-sensitive technique, in which the diffraction pattern of electrons backscattered from a sample is analysed to obtain information about the surface structure[48].

In order to achieve high temporal and momentum resolution, we use a laser-driven electron gun consisting of a nanometric tungsten tip as well as four metal electrodes (2 mm outer diameter, aperture diameter 400 µm), which act as a suppressor-extractor unit and an electrostatic einzel lens[22]. Electron pulses are generated via localized two-photon photoemission by illuminating the tip apex with femtosecond laser pulses (central wavelength 400 nm, pulse duration 45 fs, 20 nJ pulse energy) at repetition rates up to 100 kHz (note that the data presented in Figs. 2b and 3d was recorded at a repetition rate of 25 kHz while all other ULEED measurements were carried out at a repetition rate of 100 kHz). The needle cathode provides a reduced electron beam emittance allowing for a momentum-resolution in diffraction of 0.03 $Å^{-1}$. Moreover, we lower the dispersion-induced electron pulse broadening effect by decreasing the propagation length between the electron source and the sample. In this respect, the reduced dimensions of the electron gun allow for operational distances of a few millimeters at a reasonably small fraction of shadowed electron diffraction signal, resulting in electron pulse durations down to 16 ps (depending on gun-sample distance)[22]. The backscattered electrons from the surface are amplified and recorded by a combination of a chevron micro-channel plate (MCP), a phosphor screen and a cooled sCMOS camera resulting in typical integration times of t_{int} = 20 s per frame in time-resolved measurements.

In ULEED pump-probe experiments (Fig. 1c), the surface structure is excited by ultrashort light pulses (λ_c = 1030 nm, $\hbar\omega_1$ = 1.2 eV, $\Delta\tau$ = 212 fs) from a Yb:YAG amplifier system and probed by electron pulses (E_{kin} = 80 eV) at a variable time delay $\Delta t_{p\text{-}el}$. To ensure a homogeneous excitation of the area probed by the electrons, we expand the optical pump beam to (297±13) µm × (223±14) µm in the sample plane, which is significantly larger than the focal spot size of the electron gun (< 80 µm × 80 µm). Note that the electron beam diameter corresponds to at least hundreds of structural correlations lengths (taken from STM data, see, e.g. Refs.[36,49,50]), thus averaging over a large ensemble of local configurations.

For the coherent control of the structural phase transition between the (4×1) and the (8×2) phase (Fig. 2a,b; Fig. 3d), we use two pump pulses with distinct central wavelengths (P_1: $\lambda_c = 1030$ nm, $\hbar\omega_1 = 1.2$ eV, $\Delta\tau = 212$ fs; P_2: $\lambda_c = 800$ nm, $\hbar\omega_2 = 1.55$ eV, $\Delta\tau = 232$ fs) from the amplifier system and an optical parametric amplifier (OPA) to avoid interference effects around time-zero (coherent artifacts). The P_1 and P_2 beams are aligned collinearly and subsequently focused onto the sample by a single lens (see Extended Data Fig. 1a). To determine the temporal overlap of the pump pulses, we perform cross-correlation measurements using a fast nonlinear photodiode (GaP) (see Extended Data Fig. 1b). A sketch of the experimental setup is depicted in Extended Data Fig. 1a.

Optical pump-probe setup. To investigate the optical absorption modulation caused by structural modes of the indium monolayer, we use an optical pump-probe setup to measure the transient reflectivity of the In/Si(111) surface (see Extended Data Fig. 5). In this, a pump pulse ($\lambda_c = 1030$ nm, $f_{rep} = 100$ kHz) induces coherent phonon oscillations and the resulting reflectivity changes are monitored by a probe pulse ($\lambda_c = 800$ nm, $f_{rep} = 100$ kHz) as a function of the time-delay $\Delta t_{p\text{-}pr}$. The pump intensity is modulated at a frequency $f_{mod} = 25$ kHz by an acousto-optic modulator (AOM) synchronized to the laser system. Pump and probe pulses are colinearly focused on the sample at an incident angle $\alpha = 31°$. The reflected beam is guided through two short pass (SP) filters (2×OD4 for $\lambda > 900$ nm) and focused onto a Si photodiode (PD). The PD and reference signals are processed in a Lock-in amplifier, yielding the data presented in Fig. 3e and Extended Data Fig. 6.

Sample preparation. All experiments were carried out under ultra-high vacuum conditions (base pressure $p < 2\times10^{-10}$ mbar) in order to minimize surface defects from adsorption, which were found to have a significant influence on the formation of the low-temperature (8×2) phase as well and the lifetime of the metastable state[13,51]. The samples were prepared by flash-annealing Si(111) wafers (phosphorous doped, resistivity $R = 0.6$-2 Ω cm) at $T_{max} = 1250$ °C via direct current heating (maximum pressure during flashing was kept below $p_{max} = 2\times10^{-9}$ mbar). Evaporation of 1.2 monolayers of indium onto the resulting Si(111)(7×7) surface reconstruction at room temperature followed by subsequent annealing at $T = 500$ °C for 300 s resulted in a high-quality (4×1) phase,

as verified in our ultrafast LEED setup. After inspection of the (4×1) phase, the samples were immediately cooled down to a base temperature of $T = 60$ K using an integrated continuous flow helium cryostat. The phase transition between the high-temperature (4×1) and the low-temperature (8×2) phase was observed at 125 K. LEED images of the (7×7), the (4×1) and the (8×2) structure are shown in Extended Data Fig. 2.

Data analysis. The LEED pattern of the (8×2) phase from Fig. 1a and the cutouts shown in Fig. 1b were recorded at a base temperature of $T = 60$ K (cutout of the (4×1) phase: $T = 300$ K) with an integration time of $t_{int} = 60$ s. The diffraction images are plotted on a logarithmic colour scale to enhance the visibility of the twofold streaks, which are typically one order of magnitude weaker than the (8×2) spots. The location of the cutout regions within the complete diffraction image is indicated by the white rectangle in Fig. 1a.

For the analysis of single-, and double-pump ULEED experiments, we sum up the background-corrected raw data peak intensities within circular areas of interest (radius r) around the selected (4×1) and (8×2) spots. To this end, the background is determined within a ring (width dr) around the edge of each area of interest. We use radii of $r = 0.10$ Å^{-1} (40 pixels) for the fluence-dependent data presented in Fig. 2a, $r = 0.08$ Å^{-1} (30 pixels) for the data presented in Figs. 2b/3d and a ring width of d$r = 0.008$ Å^{-1} (3 pixels) for all datasets. The indices of the analysed spots are listed in Extended Data Fig. 4b.

To determine the relative changes in the (4×1) and (8×2) spot intensities caused by a single optical pulse (see Fig. 1c), the integrated peak intensities for a saturated suppression/enhancement ($\Delta t_{p\text{-}el} = 75$ ps) are normalized to the value before time-zero. This delay was chosen to account for the finite electron pulse duration under the conditions of the experiment ($\Delta t_{p\text{-}el} \approx 50$ ps). We consider potential contributions of cumulative heating effects by recording the intensities of both (4×1) and (8×2) diffraction spots as a function of the sample base temperature T_b (see Extended Data Fig. 3a). For the highest relevant fluence value ($F \approx 1.35$ mJ cm^{-2}), we find a moderate increase of T_b to a maximum temperature of 82 K, which is well below T_c.

The fluence-dependent enhancement/suppression of the (4×1)/(8×2) signal in the pump-pump-probe experiments (see Fig. 2a) is shown relative to the intensity $I(\Delta t_{p\text{-}el} = 75$ ps, $F_{1030} = 0$, $F_{800} = 0)$

without optical excitation. Concerning Figs. 2b and 3d, we define the relative switching efficiency as

$$E_s(\Delta t_{p-p}) = 1 - \frac{(I_{8\times2}(\Delta t_{p-p}) - \langle I_{8\times2}(\Delta t_{p-p} > \Delta t^*_{p-p})\rangle)}{\langle I_{8\times2}(\Delta t_{p-p} > \Delta t^*_{p-p})\rangle} \quad (1)$$

with $\Delta t_{p\text{-}p}$* = 10 ps/17 ps in Fig. 2b/3d, respectively. In all cases, $\Delta t_{p\text{-}p}$* is significantly larger than the temporal overlap of the two optical pulses given by their cross-correlation, and the damping constant of the coherent phonon oscillations.

Fourier analysis. We use super-gaussian windows in the time-domain to isolate the relevant sections in our datasets and reduce numerical artefacts of the fast Fourier transform (FFT):

$$F_{filt,t} = exp\left(-\left(\frac{(t-t_{shift})^2}{2\sigma_t^2}\right)^3\right) \quad (2)$$

The values of σ_t and t_{shift} used to create the respective figures are given below. Figure 2b: σ_t = 3.2 ps, t_{shift} = 4.5 ps; Fig. 3d: σ_t = 4.9 ps, t_{shift} = 6.5 ps; Fig. 3e: σ_t = 3.5 ps, t_{shift} = 4 ps. To extract the contributions of the individual modes to the signal from Fig. 2b, a super-gaussian frequency window

$$F_{filt,f} = exp\left(-\left(\frac{(f-f_c)^2}{2\sigma_f^2}\right)^3\right) \quad (3)$$

is employed to filter the relevant frequency range in the FFTs. The data shown in Fig. 2b (bottom) is obtained by an inverse FT of the filtered Fourier transform (shear mode: f_c = 0.5 THz, σ_f = 0.10 THz (frequency range: 0.37-0.63 THz); rotation mode: f_c = 0.9 THz, σ_f = 0.07 THz (frequency range: 0.80-0.99 THz); DC: f_c = 0.0 THz, σ_f = 0.14 THz (frequency range: 0-0.19 THz)). Here, f_c and σ_f denote the center frequency and width of the respective Fourier window. In order to study the delay-dependent frequency change of both the shear and the rotation mode, we perform a short-time Fourier transform (STFT) of the dataset depicted in Fig. 3d (bottom), again with a super-gaussian window function in the time-domain (σ_t = 3.6 ps, see Eq. 2), yielding the data shown in Fig. 3d (top).

Reflectivity and absorption of the indium monolayer. To relate the reflectivity changes measured by OPP to the absorption of the atomic indium wires, we follow Ref.[41] for the optical properties of an ultrathin layer on top of a dielectric substrate. In our case, the silicon substrate has an essentially real (and comparatively large) refractive index (n_s=3.67+0.005 i; λ=800 nm). For normal incidence, the reflection and transmission coefficients r_0 and t_0 of the bare substrate are the standard expressions:

$$r_0 = \frac{(1-n_s)}{(1+n_s)}; \quad t_0 = \frac{2}{(n_s+1)}. \quad (4)$$

Thus, the reflected wave is phase-shifted by 180°, and the transmitted wave is not phase-shifted. Furthermore, since the sheet conductivity σ^s of a monolayer satisfies $|Z_0\sigma^s| \ll |n\text{-}1|$ (Z_0: free-space impedance), the monolayer-induced changes in transmission and reflection are both proportional to the real part of σ^s, as is the absorption A of the layer:

$$\Delta R = |r_0|^2 \left(\frac{4}{n_s^2-1}\right) Re(Z_0\sigma^s) = -\frac{4(1-n_s)}{(1+n_s)^3} Re(Z_0\sigma^s), \quad (5)$$

$$\Delta T = -Re(n_s)|t_0|^2 \left(\frac{2}{1+n_s}\right) Re(Z_0\sigma^s) = -Re(n_s)\frac{8}{(1+n_s)^3} Re(Z_0\sigma^s), \quad (6)$$

$$A = \frac{4}{|1+n_s|^2} Re(Z_0\sigma^s). \quad (7)$$

In other words, due to the large real and very small imaginary part of the substrate refractive index, the imaginary part of the sheet conductivity leads to only negligible (quadrature) components in the reflected and transmitted waves. The presence of the monolayer results in a ratio of reflectance change to layer absorption of $\Delta R/A=(n_s\text{-}1)/(n_s+1)$=0.57. For the mechanism of absorption modulation (active for the rotation mode), pump-induced variations of the sheet conductivity $\delta\sigma^s$ by coherent phonons will induce variations in reflectance (δR) and absorption (δA) following the same ratio $\delta R/\delta A=\Delta R/A$. Thus, transient reflectivity (OPP) directly measures the impact of a specific phonon mode on absorption.

Relating ULEED and OPP data. From the above, variations of layer absorption lead to proportional changes in reflectance, with a prefactor that depends on the total absorption of the monolayer. This allows us to estimate the monolayer absorption, assuming absorption modulation as the sole mechanism for the rotation mode. At an identical fluence of the first excitation (see Fig. 3d/e), for the rotation mode oscillation, we measure relative changes in reflectance $(\delta R/R)_{rot}=8\cdot10^{-5}$ and modulations of the ULEED intensity δI of 0.8 % (intensity I normalized to

value at negative times). The steepness of the fluence-dependent intensity (see Fig. 1c) $F_{th} \cdot (dI/dF)|_{F,th} \approx 1.7$ at the threshold fluence F_{th}=1 mJ cm^{-2} is used to determine the relative changes in absorption of $\delta A/A$=0.47 % via $(\delta A/A)_{rot}=(1/F_{th}) \cdot ((dI/dF)|_{F,th})^{-1} \cdot (\delta I/I)_{rot}$. From these values, we obtain an estimate of the total absorption of the monolayer of

$$A \approx R \cdot \left(\frac{\delta R}{R}\right)_{rot} \cdot \left(\frac{\delta A}{A}\right)_{rot}^{-1} \cdot \left(\frac{\Delta R}{A}\right)^{-1} \approx 1\%. \quad (8)$$

This value is of the same order as a recent estimate by Frigge *et al.*[14] (0.5 %), again indicating that absorption modulation is a reasonable explanation for the rotation mode contribution to the switching efficiency.

In turn, the observed differences in rotation and shear mode amplitudes between ULEED and OPP are significant and point to a microscopic origin. In addition to possible ballistic contributions, this includes atomic-scale sample inhomogeneities such as local variations in barrier height.

References

47. Storeck, G., Vogelgesang, S., Sivis, M., Schäfer, S. & Ropers, C. Nanotip-based photoelectron microgun for ultrafast LEED. *Struct. Dyn.* **4**, 044024 (2017).
48. Van Hove, M. A., Weinberg, W. H. & Chan, C.-M. *Low-Energy Electron Diffraction: Experiment, Theory and Surface Structure Determination*. (Springer-Verlag, 1986).
49. Terada, Y. *et al.* Optical doping: active control of metal−insulator transition in nanowire. *Nano Lett.* **8**, 3577–3581 (2008).
50. Snijders, P. C. & Weitering, H. H. Colloquium: Electronic instabilities in self-assembled atom wires. *Rev. Mod. Phys.* **82**, 307–329 (2010).
51. Klasing, F. *et al.* Hysteresis proves that the In/Si(111) (8×2) to (4×1) phase transition is first-order. *Phys. Rev. B* **89**, 121107 (2014).

Data availability

The data that support the findings of this study are available on request from the corresponding author (C.R.).

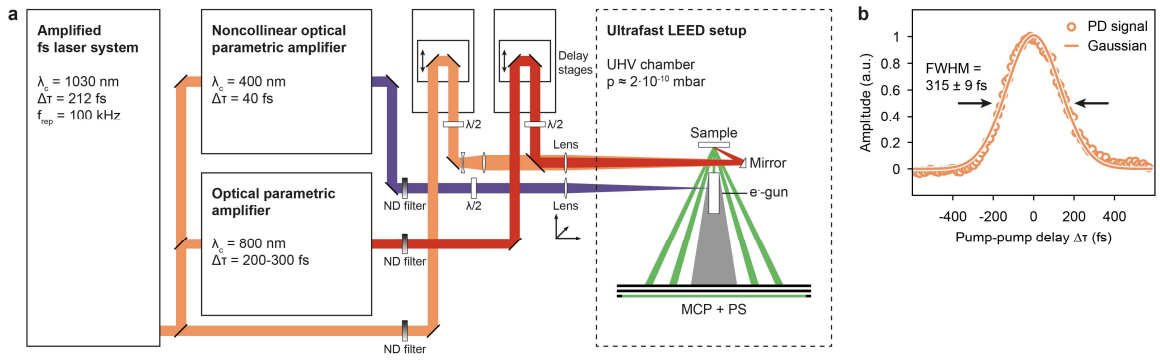

Extended Data Figure 1 | ULEED setup.

a, Ultrashort laser pulses (P_1: $\lambda_c = 1030$ nm, $\Delta\tau = 212$ fs) from an Yb:YAG amplifier (left) pump a non-collinear OPA (output: $\lambda_c = 400$ nm, $\Delta\tau = 40$ fs) and an OPA (output: P_2, $\lambda_c = 800$ nm, $\Delta\tau = 232$ fs). The 1030 nm and 800 nm beams are independently attenuated and collinearly focused onto the sample by a single lens (400 mm focal length). The relative on-axis position of the two foci is controlled by adjusting the divergence of the 1030 nm beam. The UV pulses are focused onto the tungsten needle emitter inside the electron gun (e^--gun) to generate ultrashort electron pulses. The relative timing between the electron probe and each of the two optical pump pulses is controlled independently by two separate optical delay stages. The pump-induced changes in the LEED pattern are recorded using a micro-channel plate assembly. **b**, Cross-correlation of the two pump pulses recorded with a nonlinear photodiode to determine the temporal resolution of the pump-pump-probe experiment.

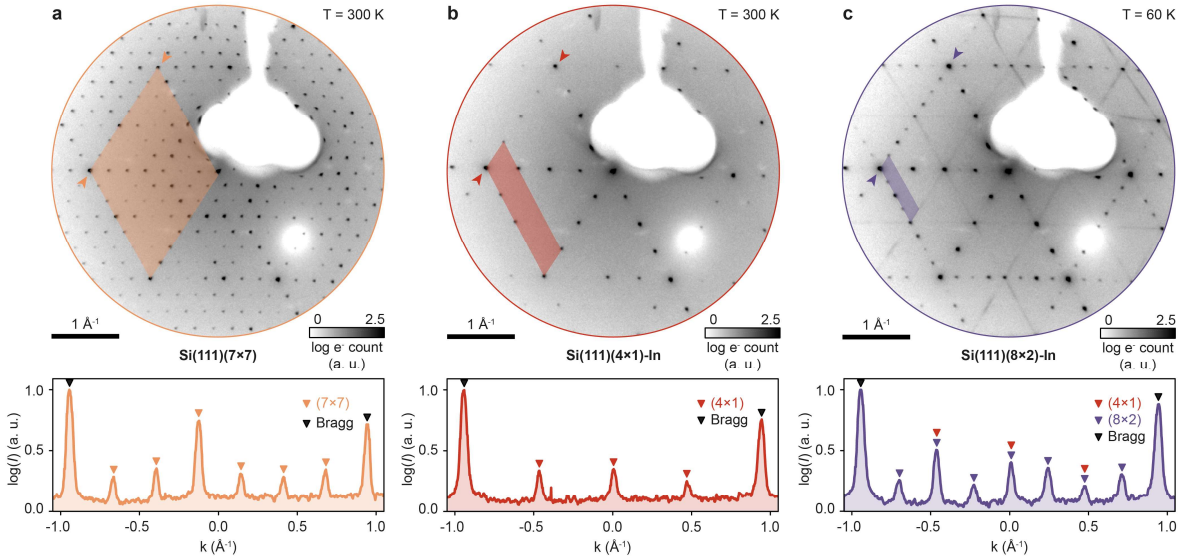

Extended Data Figure 2 | Diffraction images.

Diffraction images and lineouts of the clean (7×7)-reconstructed Si(111) surface (a), the (4×1) (b) and (8×2) phase (c) recorded in our ultrafast LEED setup (E_{kin} = 130 eV). Coloured areas correspond to the unit cells in reciprocal space, arrows indicate the location of the lineouts shown below. In the transformation from the (4×1) to the (8×2) phase, the unit cell is doubled in both dimensions. The two-fold streaks in the diffraction pattern of the (8×2) phase originate from a weak coupling between the atomic chains. The diffraction patterns of the indium-reconstructed phases feature contributions from three domains rotated by 120 degrees with respect to each other, since the hexagonal structure of the underlying substrate allows for three different orientations of the atomic Indium chains.

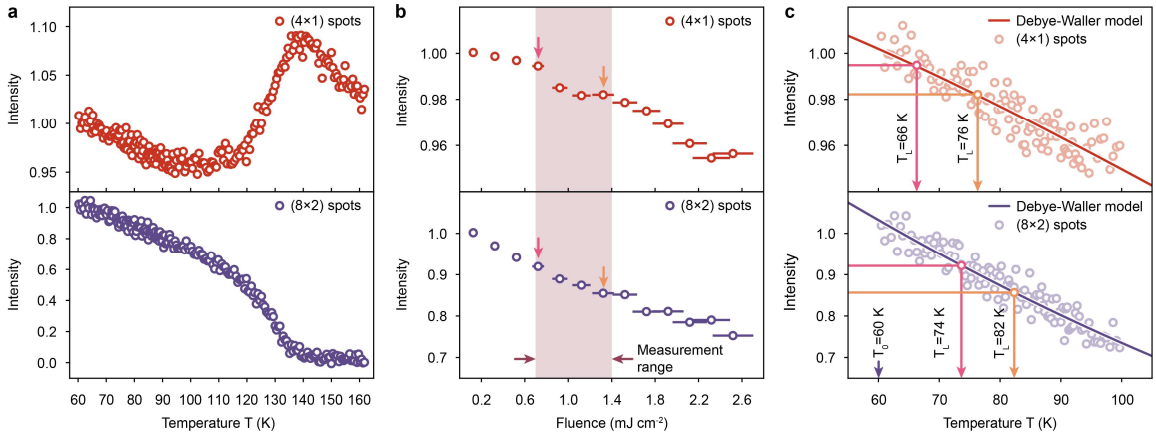

Extended Data Figure 3 | Temperature calibration.

a, Temperature-dependent integrated intensities of (4×1) (top) and (8×2) (bottom) diffraction spots across the phase transition ($T_c \approx 125$ K). **b**, Integrated diffraction spot intensities for $\Delta t_{p\text{-}el}<0$ in Fig. 1c as a function of incident fluence. **c**, Temperature calibration: A Debye-Waller model is fitted to the diffraction spot intensities in (a) between 60 K < T < 100 K. Comparing the suppressions in (b) and (c), we find a maximum temperature increase $\Delta T_b \approx 22$ K for the highest fluence value ($F_{max} \approx 1.35$ mJ cm²) within our measurement range. Note that the resulting base temperature $T_b = 82$ K is well below the T_c.

a

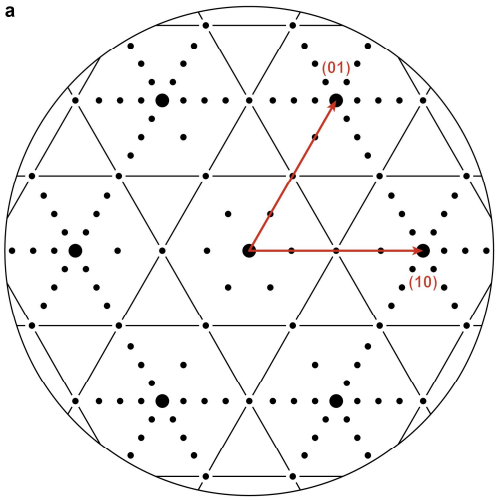

b

Pump-probe measurements (Fig.1) and static heating (Extended Data Fig.3)		
(4×1)	[(1 3), (2 2), (4 -4), (2 -4), (-2 -2), (0 -4), (0 -2), (0 -1), (-2 2)]	×1/4
(8×2)	[(3 5), (5 3), (8 -3), (5 -8), (3 -8), (-5 -3), (-8 -5)]	×1/8
Double-pulse measurements (Fig.2a)		
(4×1)	[(1 3), (2 2), (4 -4), (2 -4), (-2 -2), (3 1), (0 4)]	×1/4
(8×2)	[(3 5), (5 3), (8 -3), (5 -8), (3 -8), (-5 -3), (-8 -5), (-5 8)]	×1/8
Double-pulse measurements (Fig.2b and Fig.3d)		
(4×1)	[(1 3), (3 1), (4 0), (4 -1), (4 -4), (2 -4), (0 -4), (-1 -3), (-2 -2), (-3 -1), (-4 2), (-3 4), (-2 4), (-2 2), (-3 0), (-2 0), (0 -2), (0 -1), (2 -2), (3 -3)]	×1/4
(8×2)	[(3 5), (5 3), (8 -3), (8 -5), (3 -8), (5 -8), (3 -5), (-5 -3), (-8 3), (-8 5), (-5 8), (-3 8)]	×1/8

Extended Data Figure 4 | Definition of basis vectors and diffraction spot indexing

a, Schematic LEED pattern of the (8×2) phase and basis vectors (red) of the reciprocal lattice used to index the diffraction spots. Complete list of diffraction spots used in analysis.

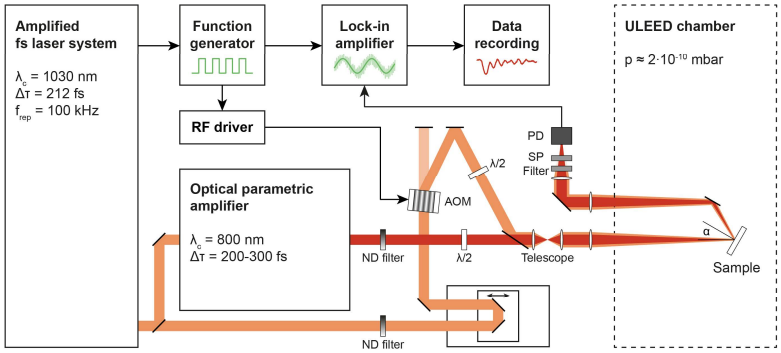

Extended Data Figure 5 | Optical pump-probe setup.

a, Ultrashort laser pulses (P_1: $\lambda_c = 1030$ nm, $\Delta\tau = 212$ fs, "Pump") from an Yb:YAG amplifier (left) pump an OPA (output: P_2, $\lambda_c = 800$ nm, $\Delta\tau = 232$ fs, "Probe"). The intensity of the pump beam is modulated at a frequency of 25 kHz by an acousto-optic modulator (AOM). Pump and probe beams are independently attenuated and collinearly focused onto the sample by a single lens (200 mm focal length). The relative on-axis position of the two foci can be adjusted using a telescope assembly. The reflected beams pass two short-pass filters blocking the pump pulses and are focused on a Si photodiode (PD). The relative timing between pump and probe pulses is controlled by an optical delay stage. The pump-induced reflectivity changes of the sample are measured by processing the PD and reference signals in a Lock-in amplifier.

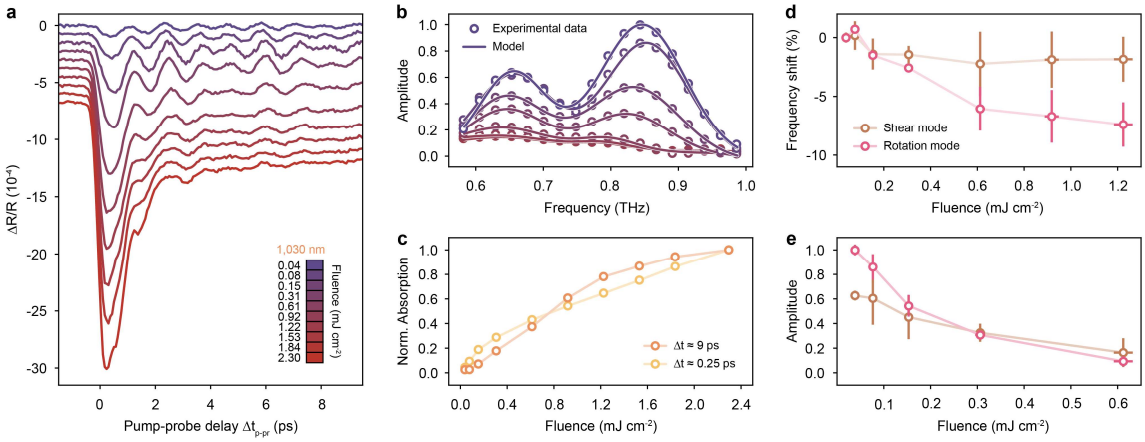

Extended Data Figure 6 | Ultrafast absorption modulation

a, Reflectivity change $\Delta R/R$ of the In/Si(111) surface as a function of the time-delay $\Delta t_{p\text{-}pr}$ between pump (1030 nm) and probe pulses (800 nm; $F = 0.14$ mJ cm^{-2}). Offsets are added to the datasets for clarity. **b**, Fourier spectra of $\Delta R/R(\Delta t_{p\text{-}pr})$ for $F = 0.04$-1.22 mJ cm^{-2} revealing two main coherent contributions ($f_{0,1} = 0.65$ THz, $f_{0,2} = 0.84$ THz) to the signals in (a), attributed to the symmetric shear and rotation modes. An additional but minor lower-frequency contribution to the reflectivity cannot be excluded at this point, given the frequency resolution of the experiment. **c**, Transient ($\Delta t_{p\text{-}pr} \approx 0.25$ ps) and long-lived ($\Delta t_{p\text{-}pr} \approx 9$ ps) contributions to ΔR/R as a function of pump fluence. The data is normalized to $\Delta R/R(\Delta t_{p\text{-}pr} < 0)$ and the respective values for $F = 2.30$ mJ cm^{-2}. **d**, Fluence-dependent frequency shifts of the two modes. The rotation mode softens significantly for higher fluences (error bars, 95% CI of the fit). **e**, Normalized Fourier amplitudes of shear and rotation modes as a function of fluence.

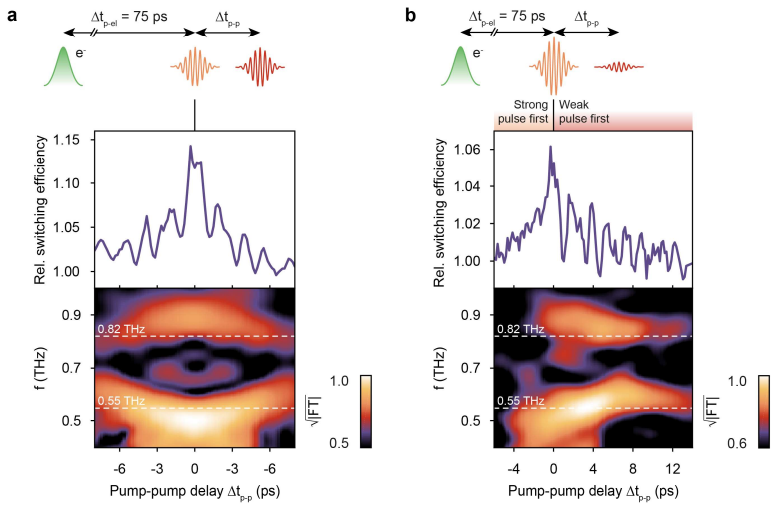

Extended Data Figure 7 | Short-time Fourier-Transforms

a, Relative switching efficiency as a function of the double-pulse delay $\Delta t_{p\text{-}p}$ (top) and short-time Fourier transform (bottom) for equal pump pulses ($F_{1030} = 0.32$ mJ cm^{-2}; $F_{800} = 0.21$ mJ cm^{-2}), revealing a pronounced softening/hardening of the shear/rotation component close to $\Delta t_{p\text{-}p} = 0$ (see also Fig. 2b). **b,** Relative switching efficiency and short-time Fourier transform for unequal pump pulses ($F_{1030} = 0.48$ mJ cm^{-2}; $F_{800} = 0.15$ mJ cm^{-2}, see also Fig. 3d).